Lattice dynamics of rare gas multilayers on the Ag(111) surface: Theory and experiment

K. D. Gibson and S. J. Sibener[a)]
Department of Chemistry and the James Franck Institute, The University of Chicago, Chicago, Illinois 60637

Burl M. Hall and D. L. Mills[b)]
Department of Physics, University of California, Irvine, California 92717

J. E. Black
Department of Physics, Brock University, St. Catharines, Ontario, Canada

(Received 14 February 1985; accepted 26 June 1985)

We discuss the lattice dynamics of argon, krypton, and xenon overlayers on the Ag(111) surface. We consider monolayer, bilayer, trilayer, and 25 layer films of each of these adsorbates. Data are also presented on the dispersion relations of selected branches of the phonon spectra of these overlayers. The data have been obtained by the method of angle-resolved inelastic He scattering. Several models of the lattice dynamics are compared with the data. It is concluded that the gas phase potentials proposed by Barker and co-workers prove suitable for a description of lateral interactions between the adsorbates, within the accuracy of the available data, provided that the phonon spectra are calculated for a lattice with the experimentally determined lattice constants.

I. INTRODUCTION

During the past two or three years, the dispersion relations of surface phonons and surface resonance modes have been studied experimentally on several crystals. Three methods have been used. The first is the inelastic scattering of highly monoenergetic beams of helium atoms from surfaces.[1] The second, neutron scattering, has been done on adsorbed monolayers, but this method only works for high surface area substrates (e.g., exfoliated graphite), and only for monolayers composed of materials with good coherent neutron scattering cross sections. Of the rare gases, only Ar^{36} falls into the latter category.[2] The third is the inelastic scattering of low energy electron beams.[3] All three techniques are very similar from the conceptual point of view, and provide us with realizations of a surface analog of the inelastic neutron scattering experiments that have played such a crucial role in elucidating the nature of elementary excitations in bulk crystals. We now have detailed data in hand on a number of alkali halide surfaces,[1] those of noble metals,[1] and both clean[3] and adsorbate covered[4,5] surfaces of transition metals.

This paper discusses data on the surface phonon dispersion curves associated with systems distinctly different in nature from those just mentioned. These are ordered overlayers of the heavy rare gases (argon, krypton, xenon) on the Ag(111) surface. The emphasis here is on the vibrational motions of the rare gas adsorbates. The rare gases are physisorbed, rather than chemisorbed on this surface. The physisorption potential well is both shallow and broad, with the consequence that the restoring force for vertical motion of the adlayer is very weak, and the associated vibrational frequency is low. At the zone boundary of the two-dimensional Brillouin zone, the phonon frequencies of these adlayers lie well *below* those of the substrate, in contrast to those associated with light chemisorbed atoms, which tend to lie well above the substrate phonon bands throughout the two-dimensional Brillouin zone.[6] Helium beams offer a unique means of probing such very soft surface phonons, whose frequencies lie below 30 cm^{-1} throughout the Brillouin zone for the systems considered here. The energy resolution available from the inelastic electron scattering method is as yet insufficient to enable resolution of these modes.

Extensive studies of such rare gas overlayers on Ag(111) have been reported by Bruch, Webb, and co-workers.[7,8] The physical picture which emerges is the following. From the perspective of the rare gas atom, the Ag(111) surface looks perfectly smooth; the substrate provides only the physisorption potential $V(z)$, which binds the rare gas atoms to the surface, and there is no evidence for any influence of the apparently very weak modulation of this potential in the two directions parallel to the surface. Thus, the adsorbates form hexagonal overlayers incommensurate with the substrate, apparently with lattice constant controlled principally by lateral interactions between the rare gas atoms. The lattice constants measured are quite close, though not precisely equal to those calculated through the use of rare gas interaction potentials deduced from gas phase data.

This paper reports data on the phonon dispersion curves of argon, krypton, and xenon monolayers, bilayers, and trilayers, on the Ag(111) surface. In addition, we report data on films formed from approximately 25 layers of adsorbate; to the helium atom, these appear very similar to semi-infinite crystals. We also present calculations of the dispersion curves of such structures for a range of models of various levels of sophistication. Throughout the paper we assume, following Webb and co-workers, that the substrate is passive, and its only role is to provide the physisorption potential $V(z)$. We then explore the sensitivity of the calculated phonon dispersion curves to variations in the lattice dynamical models, which range from the nearest neighbor central force models applied to unrelaxed multilayer structures, to calculations on fully relaxed multilayer structures, with lateral interactions modeled through use of current rare gas

[a)] Alfred P. Sloan Fellow.
[b)] Technical Report No. 84-80.

 0021-9606/85/204256-15$02.10 © 1985 American Institute of Physics

Downloaded 14 Sep 2004 to 143.106.6.126. Redistribution subject to AIP license or copyright, see http://jcp.aip.org/jcp/copyright.jsp

pair potentials extracted from gas phase data. The results are compared with the data, to test the adequacy of such pair potentials for describing lateral interactions in the adsorbed state.

We should comment on the philosophy of the theoretical analysis contained in the present paper. For the rare gas adsorbates considered here, excellent gas phase pair potentials are available, as indicated in the preceding paragraph. Of course, these pair potentials are necessarily modified somewhat in the course of adsorption. It is very difficult to estimate these changes in a quantitatively reliable manner. Also, new sources of lateral interaction can occur, such as those associated with adsorption induced dynamic electric dipole moments (whose strength is unrelated to the static dipole moments deduced from work function changes). In addition, when multilayer films are considered, the physisorption potential experienced by adsorbates in the second and third layer differs from that of adsorbates in the innermost layer, because of screening of the van der Waals interaction by the inner layers. This is also difficult to quantify reliably, at the microscopic distances of interest here. Finally, the influence of motions of substrate atoms can induce frequency shifts of the adsorbate phonons. A number of authors have explored coupling of adsorbate and substrate atom motions,[9] but the calculations are not applicable to the systems of present interest. Elsewhere, within a simple model, we have discussed this question explicitly[10] for the present systems. There are indeed frequency shifts produced comparable to those associated with the above mentioned corrections.

We thus proceed by inquiring whether these modifications are crucial by simply using the unmodified gas phase pair potentials to model the lateral interactions, and combining this with the Cole–Vidali form of the physisorption potential appropriate to an isolated adatom. We find, in fact, that the picture just described works very well indeed, when the experimentally measured lattice constant is employed in the calculations. We also explore the phonon spectra generated from some simpler models, such as a nearest neighbor central force model, and also use of the Lennard-Jones potential to model lateral interactions, and we find these clearly inadequate.

Section II of this paper discusses the experimental procedure and the data, and Sec. III discusses our theoretical calculations, and comparisons between theory and experiment. Section IV is devoted to conclusions which may be drawn from this work.

II. EXPERIMENTAL PROCEDURE

The surface phonon dispersion curves discussed in this paper were obtained using angle resolved inelastic He scattering as the dynamical probe. The actual time-of-flight (TOF) measurements were carried out in an ultra-high vacuum scattering apparatus having a base pressure of $\sim 2\times 10^{-10}$ Torr. In this apparatus the incident and final scattering angles can be independently varied, thus allowing the inelastic scattering TOF spectra to be collected across the entire Brillouin zone using a fixed angle of incidence. This is an important feature of the present experimental arrangement for accurately determining inelastic scattering probabilities. Detection of the scattered He atoms was accomplished using a differentially pumped quadrupole mass spectrometer, for which the crystal to ionizer distance was 14.45 cm. The angular resolution of the detector was $\sim 0.67°$. A more detailed description of the experimental apparatus and procedures will be presented elsewhere.[11]

The substrate for these experiments was a single crystal of Ag, cut and polished to within 0.5° of the (111) face, as checked by Laue x-ray back-reflection. The crystal surface was cleaned using Ar^+ ion bombardment. Cleanliness was verified using Auger spectroscopy. After annealing, the surface order and orientation were checked using H_2 diffraction. Surface coherence was also checked by analyzing the specular reflection angular profile using a 63 meV He beam. The coherence length was found to be on the order of 100 Å after annealing at 750 K. Temperature was monitored by a Chromel–Alumel thermocouple spot-welded directly to the back of the crystal. The crystal temperature was held at 25 ± 1 K for Kr and Xe measurements, and at 21 ± 1 K for Ar measurements.

A new liquid nitrogen cooled beam source was used to produce a very stable 18 meV He beam.[11] The velocity dispersion, $\Delta v/v$, at this energy was $\sim 1.1\%$. The incident beam was mechanically chopped by a rotating slotted disk having a shutter function of 3 μs FWHM. The beam was collimated to an angular divergence of 0.1°.

The thin film growth procedures developed during the early stages of these experiments were guided by the large quantity of structural and thermodynamic data that had been previously compiled for rare gas overlayers physi-

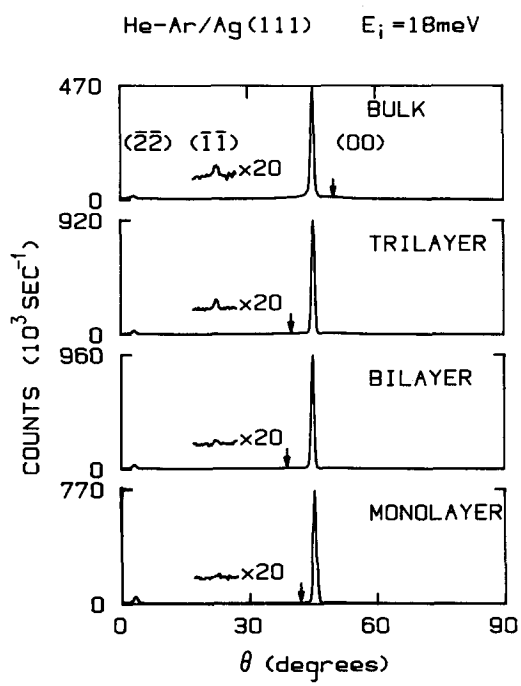

FIG. 1. Diffraction spectra for the Ar overlayers studied. Experimental results are shown for $\theta_i = 45°$ in the $(11\bar{2})$ direction, $T_s = 21$ K, and incident beam energy of 18 meV. Conditions for all of the spectra are the same, so intensities are directly comparable. Arrows indicate the final angles at which the phonon spectra of Fig. 2 were taken.

Downloaded 14 Sep 2004 to 143.106.6.126. Redistribution subject to AIP license or copyright, see http://jcp.aip.org/jcp/copyright.jsp

TABLE I. Experimental lattice constants, a_0, for the systems studied. Results are accurate to ± 0.02 Å.

Adsorbate	Monolayer a_0 (Å)	Bilayer a_0 (Å)	Trilayer a_0 (Å)	25 Layer a_0 (Å)
Ar	3.80	3.77	3.77	3.77
Kr	4.02	4.00	4.00	4.00
Xe	4.38	4.33	4.33	4.33

sorbed on Ag(111).[7,8] In particular, rare gases form azimuthally aligned but translationally incommensurate structures on this surface. Overlayers were grown using a differentially pumped dosing beam inclined at 15° to the scattering plane. A full recipe for the rather complicated process of growing good overlayers will be presented in a subsequent paper.[11] However, it is important to note that our overlayer growth procedure is not based upon thin film growth occurring at equilibrium. In brief, the Ar, Kr, and Xe monolayers were grown by controlling the dosing beam pressure and the substrate temperature. Multilayer films could then be grown on the initially deposited and carefully annealed monolayers using computer controlled dosing times and a multistep annealing procedure. The long-range order and lateral spacings were checked by elastic He diffraction; examples are shown in Fig. 1 for 1, 2, 3, and 25 layer (111) oriented films of Ar. Analysis of the specular peak widths shown in Fig. 1 indicates that all of the rare gas films have coherence lengths that are only slightly smaller than the Ag substrate, ~ 100 Å. The very low diffuse scattering occurring between diffraction peaks is another indication of the high quality of the overlayers. The experimentally derived lattice constants for each of the overlayers discussed in this paper are presented in Table I. In general, a rare gas film could be used for several hours before being discarded. When each experiment was completed, the coverage was checked using temperature programmed thermal desorption. Since the monolayer desorption peak always occurs at a higher temperature than that of the multilayers (due to the magnitude of the rare gas–Ag holding potential), the ratio of the total integrated area to the monolayer peak area was used to quantitatively measure the coverage. The TOF data collected were used only when the coverage determined fell within 10% of that expected.

Data collection was performed with a computer controlled multichannel scalar. An incident angle of 45° was used for most of the experiments reported in this paper. The entire surface Brillouin zone could be probed by varying the detector angle while holding the angle of incidence fixed. However, phonon energies under 1 meV could not be well resolved due to interference from the elastically scattered peak. Most of the TOF spectra had to be signal averaged for 1 h in order to achieve a resonable signal-to-noise ratio. This was necessitated by both the low probability of inelastic scattering, and by the high mass 4 background in the ion-pumped detector.

A nonlinear least squares routine was used to accurately fit the TOF spectra. Phonon energies were determined by comparing the peak positions of the inelastic transitions to the time-of-flight of the specular beam. Although using peak positions is not rigorously correct, the error introduced by this procedure is much smaller than the experimental uncertainty, due to the extremely narrow energy spread of the incident He beam, $\sim 200\,\mu$eV. Figure 2 presents some typical TOF spectra and fits obtained in this study. The well defined peaks indicate that single phonon exchanges are the dominant inelastic scattering channel. One, two, and three layer films clearly show an elastic component. This is attributed to crystal defects and incoherent scattering from these "soft" surfaces. The computer simulations in Fig. 2 are forward convolutions which have been scaled to show excitation line shapes, but *not* probabilities, and which (i) use as input the experimental dispersion curves, (ii) include the instrument transfer function, and (iii) assume single phonon exchanges having delta-function energy widths.

Finally, surface phonon dispersion curves were constructed by plotting the observed phonon energies vs parallel momentum. This can be accomplished in a very straightforward way using the conservation equations for total energy and crystal momentum. Figure 3 shows the results as observed along the $\overline{\Gamma}\overline{M}$ direction for Ar(111) films of increasing thickness. The dispersion curves shown in this figure clearly reveal how the surface dynamics of thin rare gas films evolve,

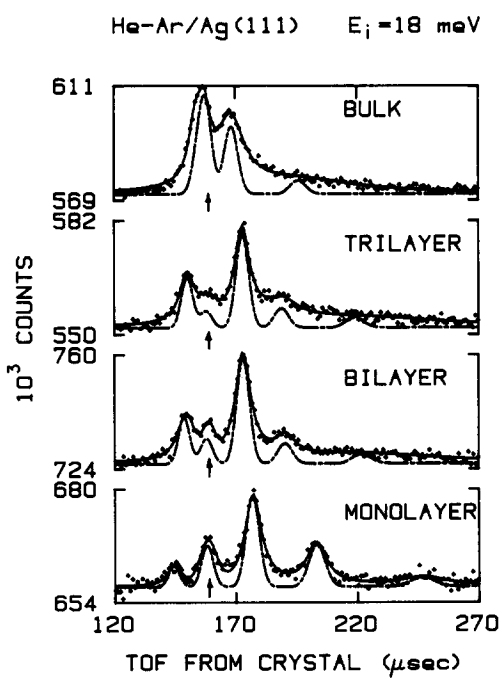

FIG. 2. TOF spectra of the Ar overlayers studied, $T_s = 21$ K, and incident beam energy of 18 meV. The dots are the experimental data, solid lines are a least-squares fit of these data, and dashed lines are computer simulations (see the text). Arrows indicate position of elastic time of flight. Spectra were taken with 1 μs channels and 1 h signal averaging.

Downloaded 14 Sep 2004 to 143.106.6.126. Redistribution subject to AIP license or copyright, see http://jcp.aip.org/jcp/copyright.jsp

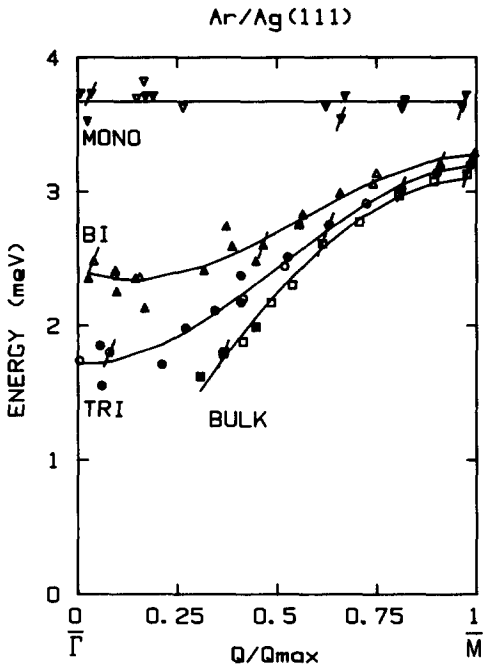

FIG. 3. Dispersion curves of the Ar overlayers from $\bar{\Gamma}$ to $\bar{M}$. Open figures are for energy loss of the beam, closed figures are for energy gain. Representative error bars are shown for energy and momentum loss features (gain and loss are with respect to the incident beam), which occured in the first zone (normal processes). Solid lines are polynomial fits to the data.

on a layer-by-layer basis, from monolayer to bulk. The monolayer mode is dispersionless (characteristic of an Einstein oscillator mode), while the bulk (25 layers) mode will be shown to be the surface Rayleigh wave. Similar dispersion curves have been measured for Kr and Xe. The comparison of the curves to the results of lattice dynamics calculations using various force laws and structures as input forms the central theme of this paper.

III. THE LATTICE DYNAMICS OF RARE GAS OVERLAYERS

The theory of lattice dynamics can calculate the dispersion curves of phonons by solving for the eigenvalues of a certain matrix, known as the dynamical matrix, at selected points $\mathbf{Q}_{\parallel}$ along the line of interest in the two-dimensional surface Brillouin zone. The eigenvalues at the point $\mathbf{Q}_{\parallel}$ are simply the squares of the phonon frequencies. In order to use the techniques of lattice dynamics, there is a certain minimum set of information needed before calculations can be done. This information falls into two classes: the first is the geometrical structure of the system (i.e., the positions of the atoms), and the second deals with the interactions between the atoms. Given this information, then lattice dynamical calculations of varying degrees of sophistication can be done.

For the rare gases on the Ag(111) surface, the gases adsorb to form ordered multilayers, as mentioned earlier. These layers have a hexagonal structure parallel to, and incommensurate with, the Ag(111) surface. Thus, for the structural inputs to the lattice dynamics, we will use a set of layers with a hexagonal lattice structure. For the trilayer case we will consider the effects of fcc stacking of the layers (*abc*) vs hcp stacking (*aba*) on the dispersion curves.

The Ag surface appears to provide primarily a support on which the rare gas crystal can be grown. The rare gas–substrate interaction is a potential with strong dependence on the height of the atom above the surface, and very weak, so far as one can see from earlier experiments, dependence on the atom's lateral position. The atom–substrate potential, $V(z)$, can be modeled as a van der Waals $1/z^3$ tail at large z combined with an exponential repulsive term at small z. This is the form that Vidali, Cole, and Klein[12] have used to derive a proposed universal physisorption potential. Following their work, we take

$$V(z) = D\,g(z^*)\,, \tag{1}$$

where $z^* = (z - z_m)/l$. Here $g(0) = -1$, so that D is the depth of the potential at the minimum, z_m is the location of the minimum of the potential (which is the position where the atoms in the monolayer sit), and l is a parameter with units of length defined by $l = (C_3/D)^{1/3}$. Here C_3 is the coefficient of the $1/z^3$ term in $V(z)$, i.e., $V(z) \to -C_3/z^3$ as $z \to \infty$ (We have taken the positive z axis to the normal to the surface and pointing into the vacuum). The functional form or $g(z^*)$ is given as

$$g(x) = \left(\frac{3}{u-3}\right) e^{-ux/a} - \frac{1}{(x+a)^3}\,. \tag{2}$$

The parameters u and a are dimensionless and are related by the condition that $g(0) = -1$.

In order to model the atom–substrate interaction, it is necessary to determine the values of D, C_3, l, a, and u. Although there are five parameters, there are only three independent ones, D, C_3, and a (or u). D has been determined experimentally by Unguris *et al.*[13] for the systems of interest here. We have chosen to use the value of C_3 calculated by Zaremba and Kohn.[14] The third piece of information that we have is the frequency of the monolayer vibrations associated with adsorbate motion normal to the surface. This is provided by the data reported in the present paper. This tells us the second derivative of $V(z)$ at its minimum. This, together with D and C_3 is sufficient to determine a and hence, u. The

TABLE II. The input parameters used to construct $V(z)$, for the three adsorbates of interest in the present paper.

Adsorbate	D (meV)	C_3 (meV Å^3)	l (Å)	u	a
Ar	66	1620	2.91	5.45	0.766
Kr	108	2259	2.76	4.77	0.718
Xe	168	3270	2.69	4.64	0.707

Downloaded 14 Sep 2004 to 143.106.6.126. Redistribution subject to AIP license or copyright, see http://jcp.aip.org/jcp/copyright.jsp

$V(z)$ has been determined, and we can then incorporate the influence of $V(z)$ on the lattice dynamics. For the three adsorbates of interest, Table II provides the parameters we have used.

With $V(z)$ now determined, we have a model of the rare gas atoms' interaction with the substrate, but before any calculations can be done, we need to know how the rare gas atoms interact with each other. If we simply wanted to model the lattice dynamics of the system, we could take a set of force constants between the rare gas atoms and determine their values by adjusting them until the measured dispersion curves have been matched. Rather than do that, we have chosen to make use of some of the excellent gas phase pair potentials that have been determined by Barker and coworkers. The potential used for argon was that described by Barker, Fisher, and Watts.[15] The potential used for krypton was the Barker K2 potential,[16] and the Barker X4 potential[16] was used for xenon. These potentials are multiparameter in nature, and reproduce a wide range of physical processes quite well. Since they have analytical forms, it is quite easy to calculate the derivatives required for the lattice dynamics. Although these potentials reproduce liquid and solid properties as well as gas phase properties well, there should be some changes in the pair potentials because of the proximity of the adsorbates to the Ag surface. However, at the current time there is no clear experimental information available on what these changes might be and available theories are quite approximate in nature. Hence we will use the unmodified pair potentials and we may then regard the comparison between our calculations and the data as a test of whether these forms

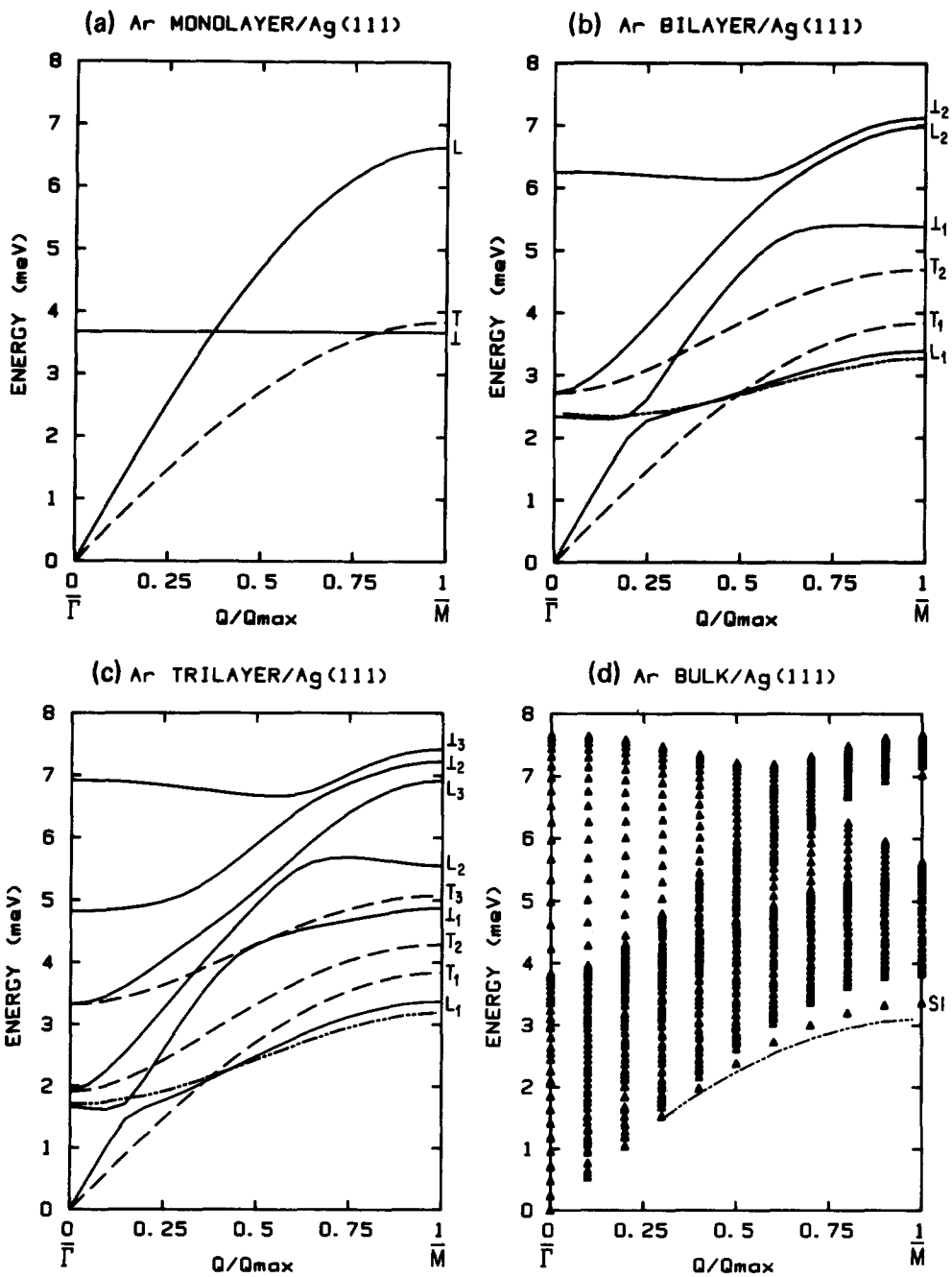

FIG. 4. For argon, we show the phonon dispersion curves calculation from model B for (a) the monolayer, (b) the bilayer, (c) the trilayer, and (d) a "bulk" crystal. The information here is synthesized from a calculation based on a 25 layer slab. For 1, 2, and 3 layers, the solid lines are calculated dispersion curves for modes polarized in the sagittal plane, the dashed line are transverse modes, and the chained line is a best fit to the data. For 25 layers, triangles are calculated dispersion curves, and the chained line is a best fit to the data.

Downloaded 14 Sep 2004 to 143.106.6.126. Redistribution subject to AIP license or copyright, see http://jcp.aip.org/jcp/copyright.jsp

may be applied to physisorbed rare gas atoms. This analysis then provides a foundation upon which a systematic study of the various factors which contribute to deviations between our calculations and the data can be based. Deviations may arise due to three body forces, such as Axilrod–Teller forces, and substrate mediated forces, such as those of McLachlan,[17] which were not included in the interaction potential. An additional factor which has been ignored in the present study is the influence that substrate motion can have on the overlayer lattice dynamics. This latter problem is under study, and we describe our results in a subsequent publication.[10]

With the structure, adsorbate–substrate, and lateral interactions between adsorbates determined as just outlined, it is now possible to do lattice dynamical calculations. We have chosen to explore three basic models, arranged in order of increasing sophistication. The first model, model A, assumes that only nearest neighbor central force interactions exist. Thus, each atom is connected by "springs" only to its nearest neighbors. The nearest neighbor spacing is that of a pair of atoms in equilibrium. The only coupling between the substrate and the rare gas lattice occurs from the first layer (the one nearest the surface), to the substrate with the spring constant k_s determined from the second derivative of $V(z)$. The rare gas–rare gas force constant k_0 is determined from the second derivative of the pair potentials, evaluated at the minimum of the potential. This is the simplest model used.

The second model, model B, again uses only nearest neighbor central forces between the rare gas atoms. Here again the nearest neighbor spacing is the same as in model A. The difference is that now every layer in the rare gas crystal is connected to the substrate by a force constant k_s (l_z),

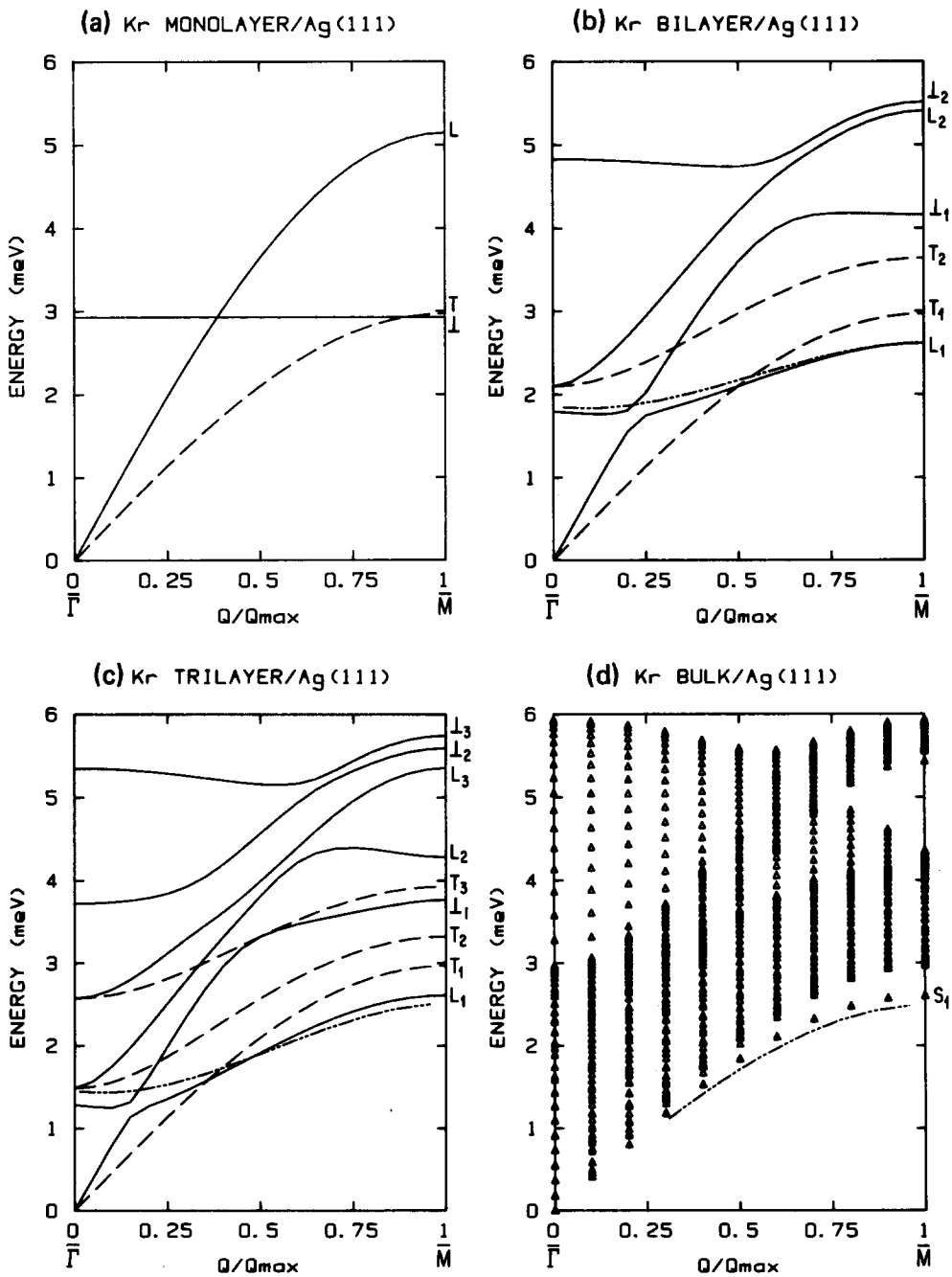

FIG. 5. For krypton, we show the phonon dispersion curves calculation from model B for (a) the monolayer, (b) the bilayer, (c) the trilayer, and (d) a "bulk" crystal. The information here is synthesized from a calculation based on a 25 layer slab. For 1, 2, and 3 layers, the solid lines are calculated dispersion curves for modes polarized in the sagittal plane, the dashed line are transverse modes, and the chained line is a best fit to the data. For 25 layers, triangles are calculated dispersion curves, and the chained line is a best fit to the data.

Downloaded 14 Sep 2004 to 143.106.6.126. Redistribution subject to AIP license or copyright, see http://jcp.aip.org/jcp/copyright.jsp

where l_z labels the layers. In model A, $k_s(l_z) = 0$ if $l_z \neq 1$. Model B takes into account the fact that the atoms in the higher layers feel $V(z)$; we compute $k_s(l_z)$ from $V(z)$.

In model C we allow all the rare gas layers to relax both parallel and normal to the silver substrate, to assume a configuration in which the static potential energy is minimized. At the same time, we also extend the effects of the Barker potentials out beyond the nearest neighbors. This is accomplished by generating the dynamical matrix by a computer routine rather than setting it up analytically. Thus any number of neighbors can be used. The model allows us to see the effects of the long-range tail of the rare gas pair potential, and also of the relaxation effects just described. The number of neighbors used is shown in a subscript to the model, in the subsequent discussion. That is, the C_5 model which includes interactions through fifth neighbors, and so on.

In Figs. 4 to 6, we show the results of the lattice dynamics calculations for the three rare gases on Ag(111). Parts a, b, c, and d show the dispersion curves for the monolayer, bilayer, and trilayer using model B, and 25 layers using model A, respectively. For 25 layers, model A will not differ appreciably from model B. The curves are qualitatively similar for all three models. We shall elaborate on the quantitative difference below. For the monolayer, the motion normal to the surface is decoupled from the motion parallel to the surface in any model within which lateral interactions between adsorbates have central force character. This property is shared by all three models. Also, the two modes that involve

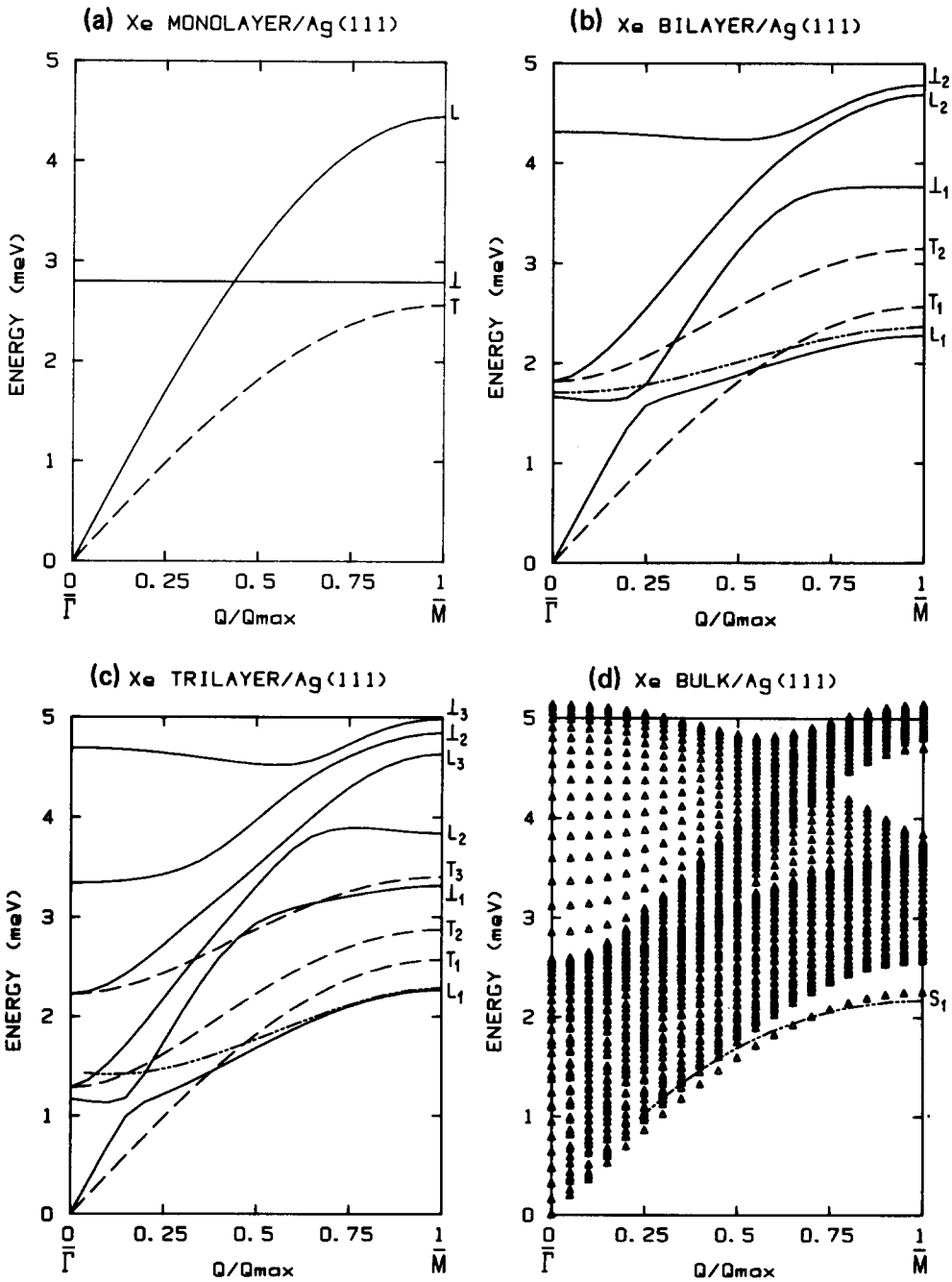

FIG. 6. For xenon, we show the phonon dispersion curves calculation from model B for (a) the monolayer, (b) the bilayer, (c) the trilayer, and (d) a "bulk" crystal. The information here is synthesized from a calculation based on a 25 layer slab. For 1, 2, and 3 layers, the solid lines are calculated dispersion curves for modes polarized in the sagittal plane, the dashed line are transverse modes, and the chained line is a best fit to the data. For 25 layers, triangles are calculated dispersion curves, and the chained line is a best fit to the data.

Downloaded 14 Sep 2004 to 143.106.6.126. Redistribution subject to AIP license or copyright, see http://jcp.aip.org/jcp/copyright.jsp

motion parallel to the surface decouple into a pure transverse mode and a pure longitudinal mode along the entire line $\overline{\Gamma}$ to $\overline{M}$. Note that the parallel modes are acoustic in nature, while the motion normal to the surface acts like an Einstein oscillator, with zero dispersion.

For the bilayer, there are six modes for each value of $\mathbf{Q}_{\parallel}$. Two of these are transverse modes and are represented by the dashed lines in the figures. The other four modes are sagittally polarized in the y–z plane, and their polarization changes as one moves along the $\overline{\Gamma}$–$\overline{M}$ line. Let us label the modes by their polarization at the $\overline{\Gamma}$ point. Then there are two longitudinal modes L_1 and L_2, and two perpendicular modes $\perp_1$ and $\perp_2$, in addition to the two transverse modes T_1 and T_2. At $\overline{\Gamma}$, T_1 and L_1 are zero frequency acoustic modes where an atom in each layer displaces by the same amount in the appropriate direction. At $\overline{\Gamma}$, the modes T_2 and L_2 have optical character, and thus the atoms in the different layers move by the same amount, but in opposite directions. The mode $\perp_1$ has atoms in the different layers all moving in the $+\hat{z}$ direction, but by different amounts, while $\perp_2$ has the atoms moving in opposite directions 180° out of phase, again with different magnitudes of displacement.

At $\overline{M}$, the situation is less simple, as the atoms in the different layers no longer move exactly in phase or out of phase. Here T_1 and T_2 remain transverse modes with the atoms having the same magnitude displacements, but now the atoms in the second layer are 120° in phase ahead of the first layer atoms in T_1, while they are 60° behind for T_2. The mode L_1 is now no longer a simple longitudinal mode. It is dominated by the motion of the second layer atoms in the $\hat{z}$ direction. In contrast to this, L_2 is still longitudinal, and is dominated by the longitudinal motion of the first layer atoms along the $\hat{y}$ direction. The model $\perp_1$ is now dominated by the motion of the first layer atoms normal to the surface, while $\perp_2$ is dominated by the longitudinal motion of the second layer atoms. For all of the sagittal modes, the other layer has some motion in the y–z plane, but over 80% of the contribution to the normalization sum $\sum_{l_z\alpha} |e_\alpha(l_z)|^2$ comes from the dominant motion. Here $\hat{e}(l_z)$ is the displacement of the atom in layer l_z, and the sum just quoted equals unity. Both L_1 and $\perp_2$ have the second layer leading the first by 120°, while L_2 and $\perp_1$ have it trailing the first layer by 60°.

The situation is different for the trilayer. Here the motions are exactly in phase or out of phase at $\overline{\Gamma}$ and also at $\overline{M}$. At $\overline{\Gamma}$, the transverse and longitudinal modes form three degenerate pairs. The first pair, T_1 and L_1, are uniform displacements of the atoms in all three layers and represent rigid body translations of the rare gas crystal. These thus have zero frequency, by virtue of the independence of $V(z)$ on the adsorbate coordinates in the plane parallel to the surface. The second pair, L_2 and T_2, are analogous to the symmetric stretching mode of a linear triatomic homonuclear molecule. The atoms in the first and third layers move with equal magnitudes and in opposite directions, while the atoms in the second layer are motionless. The last pair, T_3 and L_3, are analogs to the asymmetric stretch, as the atoms in the first and third layers move by the same amount in the same direction, while the second layer atoms move in the opposite direction with twice the displacement. The modes $\perp_1$, $\perp_2$, and $\perp_3$ all have the atoms moving along the z direction, with $\perp_1$ having all the atoms moving in the same direction by different amounts. At $\overline{M}$ T_1, T_2, and T_3 have exactly the same eigenvectors that they had at $\overline{\Gamma}$. However, L_1 is now dominated by the normal motion of the third layer atoms, while the major contribution to L_2 comes from the normal motion of the first layer atoms. Finally, L_3 has the eigenvector that L_2 had at $\overline{\Gamma}$, i.e., it is now the analog to the symmetric stretch, while $\perp_3$ is now dominated by the longitudinal motion of the second layer atoms.

As we go from 3 layers to 25 layers, we approach the case of a semi-infinite crystal. Now we see a single Rayleigh wave, above which the bulk bands are present. Note the gap in bulk bands in the vicinity of $\overline{M}$. A surface mode of primarily longitudinal polarization is present in the gap. Hints of the gap can be seen from the dispersion curves for the trilayer case.

Since the polarization changes as one moves across the zone, different branches can be responsible for exciting the experimentally observed peaks in different parts of the zone, since it is the perpendicular atomic motions that dominate the scattering cross section.

In Figs. 4 through 6, the chained lines represent a best fit to the experimental data. It should be remarked that model B does not provide the best fit to the data, but this comparison will provide an initial orientation. At $\overline{\Gamma}$, the $\perp_1$ is responsible for the peak, but as one moves along the line $\overline{\Gamma}$–$\overline{M}$, a hybridization occurs at about 1/5 of the way to $\overline{M}$, and the L_1 branch becomes the mode excited by the atoms from there to $\overline{M}$. For the Ar and Kr bilayers, there is experimental evidence for a second peak at a higher frequency. One should associate this peak with either the $\perp_1$ or the L_2 branch; we shall discuss the interpretation of this feature later.

TABLE III. Input parameters for model A used to describe the rare gas overlayers. The second column is the value of k_s provided by the Cole–Vidali potential, obtained by fitting to the measured value of the monolayer vibration normal to the surface. The two values of k_0 are deduced from the pair potentials proposed by Barker *et al.* (third column), and that determined from the Lennard-Jones potential (fourth column). The final column lists values of k_0 obtained empirically by fitting the measured phonon frequency at $\overline{M}$ for a 25 layer film to that generated by model A applied to such a slab.

Adsorbate	k_s (fit) (THz^2)	k_0 (*pp*) (THz^2)	k_0 (LJ) (THz^2)	k_0 (fit) (THz^2)
Ar	62.10	34.006	24.889	30.0
Kr	39.32	20.387	13.871	18.72
Xe	36.28	15.270	10.589	15.24

Downloaded 14 Sep 2004 to 143.106.6.126. Redistribution subject to AIP license or copyright, see http://jcp.aip.org/jcp/copyright.jsp

TABLE IV. The normal mode frequencies calculated for the various models discussed in the text, at $\bar{\Gamma}$ and $\bar{M}$ in the two-dimensional Brillouin zone of the Ar bilayer. The column A(B) are frequencies calculated for model A, with the force constant between rare gas atoms determined by the Barker gas phase potential, the column A(LJ) uses the Lennard-Jones potential to generate this force constant (see Table III), that labeled B is model B, and two versions of model C are explored. Each sums over pairs out to a distance equal to five nearest neighbors, the first (column labeled C_5) treats an unrelaxed bilayer, and one [column labeled C_5 (r)] treats a fully relaxed system. All frequencies are in meV.

	Ar Bilayer				
Modes	A (B)	A (LJ)	B	C_5	C_5 (r)
$\bar{\Gamma}$					
T_1, L_1	0.000	0.000	0.000	0.000	0.000
T_2, L_2	2.714	2.322	2.714	2.730	3.002
$\perp_1$	2.295	2.192	2.342	2.395	2.452
$\perp_2$	6.137	5.498	6.250	6.592	7.073
$\bar{M}$					
T_1	3.838	3.284	3.838	3.963	3.935
T_2	4.701	4.022	4.701	4.975	5.151
L_1	3.438	2.985	3.397	3.534	3.787
L_2	6.987	5.992	6.993	7.559	7.688
$\perp_1$	5.231	4.789	5.389	5.589	5.787
$\perp_2$	7.120	6.114	7.129	7.689	7.838

Having seen something of the nature of the different phonon branches, and how their character varies over the line $\bar{\Gamma}$–$\bar{M}$, it is useful to examine the sensitivity of the theoretical results to the input parameters and to the choice of model. We present results of our comparison of various models in the form of a sequence of tables which list frequencies at $\bar{\Gamma}$ and $\bar{M}$, because some differences are too small to show up in dispersion curve plots. Table III shows the force constants (in THz^2) used for model A, including two choices for k_0, one from the accurate pair potentials and one from the Lennard-Jones 6-12 potential, for the three rare gases. The value for k_s was defined from the experimentally measured monolayer frequency via $k_s = 2\omega^2_{\text{expt}}$, and other force constants defined in this paper are in equivalent units. That is, in the case where the force constant is proportional to the second derivative of the two particle potential, our tabulated force constants are twice this second derivative divided by the adsorbate mass. It is immediately obvious that the Barker pair potential value for k_0 is about 50% larger than the Lennard-Jones value for k_0. Hence those frequencies which depend only on k_0 should be about 20% larger for the Barker pair potential then they are for the Lennard-Jones potential. This can be seen in Tables IV through IX by comparing the columns labeled A (B) and A (LJ). Column A (B) gives the results using model A with k_0 from the accurate pair potential, while A (LJ) is the results using model A with the Lennard-Jones value for k_0. In all cases, the frequencies are low-

TABLE V. The normal mode frequencies at $\bar{\Gamma}$ and $\bar{M}$ in the two-dimensional Brillouin zone, for the Kr bilayer. The columns are labeled by the convention used in Table IV.

	Kr Bilayer				
Mode	A (B)	A (LJ)	B	C_5	C_5 (r)
$\bar{\Gamma}$					
T_1, L_1	0.000	0.000	0.000	0.000	0.000
T_2, L_2	2.102	1.733	2.102	2.116	2.321
$\perp_1$	1.813	1.704	1.795	1.837	1.881
$\perp_2$	4.786	4.200	4.830	5.103	5.470
$\bar{M}$					
T_1	2.972	2.451	2.972	3.076	3.052
T_2	3.640	3.002	3.640	3.865	4.000
L_1	2.669	2.240	2.620	2.723	2.915
L_2	5.412	4.478	5.414	5.866	5.964
$\perp_1$	4.095	3.685	4.162	4.320	4.472
$\perp_2$	5.515	4.578	5.519	5.965	6.079

TABLE VI. The normal mode frequencies at $\bar{\Gamma}$ and $\bar{M}$ in the two-dimensional Brillouin zone, for the Xe bilayer. The columns are labeled by the convention used in Table IV.

	Xe Bilayer				
Mode	A (B)	A (LJ)	B	C_5	C_5 (r)
$\bar{\Gamma}$					
T_1, L_1	0.000	0.000	0.000	0.000	0.000
T_2, L_2	1.819	1.515	1.819	1.796	1.987
$\perp_1$	1.700	1.583	1.663	1.698	1.753
$\perp_2$	4.285	3.833	4.312	4.487	4.804
$\bar{M}$					
T_1	2.572	2.142	2.572	2.615	2.591
T_2	3.150	2.623	3.150	3.290	3.417
L_1	2.335	1.971	2.285	2.345	2.528
L_2	4.692	3.920	4.693	4.994	5.087
$\perp_1$	3.725	3.386	3.764	3.860	3.973
$\perp_2$	4.786	4.037	4.790	5.080	5.199

TABLE VII. The normal mode frequencies at $\bar{\Gamma}$ and $\bar{M}$ for the Ar trilayer, for the three models explored in this work. We also calculate the frequencies for a trilayer with hcp stacking arrangement aba, rather than the fcc arrangement abc. This has been done for model A and model C_5, and the results for each are in the columns labeled A (hcp) and C_5 (hcp). See the caption of Table IV for the remaining conventions.

	Ar Trilayer						
Mode	A (B)	A (hcp)	A (LJ)	B	C_5	C_5 (r)	C_5 (hcp)
$\bar{\Gamma}$							
T_1, L_1	0.000	0.000	0.000	0.000	0.000	0.000	0.000
T_2, L_2	1.919	1.919	1.642	1.919	2.017	2.012	2.039
T_3, L_3	3.324	3.324	2.844	3.324	3.494	3.491	3.494
$\perp_1$	1.666	1.666	1.546	1.674	1.762	1.770	1.750
$\perp_2$	4.713	4.713	4.263	4.826	5.188	5.139	5.133
$\perp_3$	6.885	6.885	6.003	6.919	7.752	7.770	7.751
$\bar{M}$							
T_1	3.839	3.838	3.284	3.838	4.109	4.109	4.109
T_2	4.292	4.291	3.671	4.292	4.711	4.709	4.720
T_3	5.078	5.078	4.344	5.078	5.618	5.616	5.618
L_1	3.387	3.387	2.913	3.381	3.603	3.551	3.665
L_2	5.401	5.461	4.890	5.548	6.041	6.065	6.192
L_3	6.920	6.920	5.920	6.919	7.866	7.865	7.834
$\perp_1$	4.824	4.824	4.260	4.882	5.260	5.244	5.016
$\perp_2$	7.231	7.231	6.193	7.228	8.234	8.234	8.248
$\perp_3$	7.416	7.416	6.364	7.424	8.400	8.402	8.397

Downloaded 14 Sep 2004 to 143.106.6.126. Redistribution subject to AIP license or copyright, see http://jcp.aip.org/jcp/copyright.jsp

TABLE VIII. The normal mode frequencies at $\bar{\Gamma}$ and $\bar{M}$ for the Kr trilayer, for the three models used. The columns are labeled by the convention used in Table VII.

	Kr Trilayer						
Mode	A (B)	A (hcp)	A (LJ)	B	C_5	C_5 (r)	C_5 (hcp)
$\bar{\Gamma}$							
T_1, L_1	0.000	0.000	0.000	0.000	0.000	0.000	0.000
T_2, L_2	1.486	1.486	1.226	1.486	1.554	1.539	1.568
T_3, L_3	2.574	2.574	2.123	2.574	2.691	2.669	2.691
$\perp_1$	1.310	1.310	1.188	1.281	1.357	1.358	1.349
$\perp_2$	3.683	3.683	3.259	3.722	4.011	3.959	3.974
$\perp_3$	5.345	5.345	4.531	5.348	5.976	5.949	5.975
$\bar{M}$							
T_1	2.972	2.972	2.451	2.972	3.167	3.170	3.167
T_2	3.323	3.323	2.741	3.323	3.636	3.630	3.642
T_3	3.932	3.932	3.243	3.932	4.338	4.323	4.338
L_1	2.625	2.625	2.178	2.617	2.773	2.722	2.823
L_2	4.253	4.253	3.748	4.281	4.661	4.661	4.77
L_3	5.358	5.358	4.419	5.358	6.067	6.063	6.043
$\perp_1$	3.761	3.761	3.205	3.769	4.057	4.026	3.872
$\perp_2$	5.599	5.599	4.626	5.595	6.349	6.334	6.359
$\perp_3$	5.744	5.744	4.761	5.747	6.477	6.467	6.475

er in the column A (LJ) than those in column A for the same branch, and the Lennard-Jones results are in clear disagreement with experiment.

Another interesting issue is the lateral position of the top layer in the trilayer. Does it sit over the hcp or fcc site? Bulk rate gas crystals form fcc lattices,[18] but it might be possible for the layer to sit in the hcp site for the trilayer system, particularly when one considers that energy differences between the bulk hcp and bulk fcc structure are very small. The results for the hcp site calculations can be seen in Tables VII to IX under the column A (hcp), and also that labeled C_5 (hcp). Notice that at $\bar{\Gamma}$ and $\bar{M}$ there is no difference between the frequencies that lattice dynamics predicts for the fcc and the hcp models, using model A, and only small changes in model C. As one moves away from these high symmetry points toward the center of the line $\bar{\Gamma}$–$\bar{M}$, then some small differences appear, but the differences are so small that the experiment cannot resolve them at present. Thus we can make no decision on this question at the present time.

When the atom–surface potential is allowed to influence the atoms in the higher layers, and not only that closest to the surface, it creates a driving force to cause relaxation between the rare-gas overlayers. This driving force moves the higher planes inward, away from their perfect crystal positions. If k_0 is held fixed, then the resulting changes to the dispersion curves are small and occur mainly in the transverse modes, which have not yet been seen experimentally. More important are the changes in the dynamical matrix for the higher layers caused by $V(z)$. The one parameter which is undetermined in the Cole and Vidali form of $V(z)$ is z_m, the location of the potential minimum. This presents no problem for the monolayer, as it must sit at z_m. Hence we can choose the minimum to be the origin ($z = 0$) and the value of z_m is irrelevant. But for multilayer structures, we must allow the layers to relax, and the innermost layer no longer sits at a minimum of $V(z)$. We have performed a simple calculation to get a rough idea of the amount of interlayer relaxation that occurs. We have calculated the energy per unit cell by summing the pair potentials over shells of atoms until the sum converges, and then added the contribution from $V(z)$. We varied the two-dimensional lattice constant a_0 and the location of the layers to locate the minimum in the total energy. The results are summarized in Table X. As might be expected, the first layer is pushed closer to the substrate by the layers above it. Knowing the position of the layers, it is then possible to calculate the force constant acting on that layer from $V(z)$. The k_s (l_z) are shown in Table XI. Their effect can be seen in Tables IV through IX under the column labeled B. Note that in model B the interplanar spacings are not changed, only the forces connecting the planes to the sub-

TABLE IX. The normal mode frequencies at $\bar{\Gamma}$ and $\bar{M}$ for the Xe trilayer, for the three models used. The columns are labeled by the convention used in Table VII.

	Xe Trilayer						
Mode	A (B)	A (hcp)	A (LJ)	B	C_5	C_5 (r)	C_5 (hcp)
$\bar{\Gamma}$							
T_1, L_1	0.000	0.000	0.000	0.000	0.000	0.000	0.000
T_2, L_2	1.286	1.286	1.071	1.286	1.311	1.328	1.324
T_3, L_3	2.228	2.228	1.855	2.228	2.270	2.303	2.270
$\perp_1$	1.203	1.203	1.082	1.171	1.224	1.238	1.214
$\perp_2$	3.321	3.321	2.959	3.342	3.522	3.528	3.491
$\perp_3$	4.691	4.691	4.055	4.694	5.099	5.180	5.098
$\bar{M}$							
T_1	2.572	2.572	2.142	2.572	2.675	2.670	2.675
T_2	2.876	2.876	2.395	2.876	3.075	3.082	3.080
T_3	3.403	3.403	2.833	3.403	3.670	3.694	3.670
L_1	2.280	2.280	1.908	2.271	2.358	2.362	2.387
L_2	3.809	3.809	3.440	3.838	4.044	4.083	4.134
L_3	4.637	4.637	3.861	4.637	5.124	5.128	5.106
$\perp_1$	3.329	3.329	2.825	3.316	3.530	3.552	3.394
$\perp_2$	4.850	4.850	4.047	4.846	5.366	5.393	5.370
$\perp_3$	4.983	4.983	4.184	4.986	5.478	5.502	5.477

TABLE X. The effect on static properties of the bilayers and trilayers of extending the influence of $V(z)$ beyond the layer closest to the substrate. Here in the first column $z(1)$ is the position of the innermost layer, measured relative to z_m, d_{12}, and d_{23} are the spacings between the first and second, and the second and third layers, respectively, and a_0 is the lattice constant calculated for the structure. The last column gives the experimentally measured lattice constants.

Bilayer Adsorbate	$z(1)$ (Å)	d_{12} (Å)	a_0 (Å)	a_0 (Å), expt.
Ar	−0.05	3.00	3.73	3.77
Kr	−0.05	3.19	3.97	4.00
Xe	−0.05	3.47	4.33	4.33

Trilayer Adsorbate	$z(1)$ (Å)	d_{12} (Å)	a_0 (Å)	d_{23} (Å)	a_0 (Å), expt.
Ar	−0.05	3.02	3.71	3.04	3.77
Kr	−0.06	3.22	3.95	3.24	4.00
Xe	−0.05	3.50	4.31	3.52	4.33

Downloaded 14 Sep 2004 to 143.106.6.126. Redistribution subject to AIP license or copyright, see http://jcp.aip.org/jcp/copyright.jsp

TABLE. XI. The force constant k_s (l_z) (in THz^2) for the various layers, generated by $V(z)$ after the structures are fully relaxed.

Adsorbate	No. of layers	k_s (1)	k_s (2)	k_s (3)
Ar	1	62.171		
	2	71.955	−2.357	
	3	71.955	−2.317	−0.248
Kr	1	39.379		
	2	42.656	−1.649	
	3	43.239	−1.620	−0.151
Xe	1	36.978		
	2	38.798	−1.288	
	3	38.798	−1.255	−0.105

strate are altered. It can be seen that only those modes with vibration normal to the surface are affected, when these results are compared with column A. The degree to which they are affected depends directly on the amount of normal vibration they have, hence the L_1 and $\perp_1$ modes are the most strongly affected.

Since the rare gas pair potentials are fairly long ranged, one must inquire about the role of distant neighbor interactions. We thus turn to a discussion of the calculations based on model C. It was found that the convergence was very rapid, as we included progressively more neighbors. The most important change, however, was the fact that this method incorporates changes in the nearest neighbor distances. In the nearest neighbor models A and B, the atoms within a given plane have as their equilibrium position the minimum of the pair potential. Hence k_0 is calculated from the second derivative of the pair potential evaluated at its minimum. When we use model C, the atoms are no longer at the minimum. They are at the locations shown in Table X. The lattice constant is smaller than the distance at which the pair potential has its minimum, since the lattice can lower its total energy this way. Table XII shows the difference that this makes for the Ar bilayer by going from model B, to model C_1 (nearest neighbors, but with a new k_0). We see that the frequencies are raised (with the increased k_0) at the reduced separation of the atoms. As we add more neighbors to the calculation of model C we see the frequencies are now reduced from the values given by model C_1. Note that convergence is rapid, and that by the time five neighbors have been used, the frequencies have converged to four figures. Finally, we present in Table XIII the normal mode frequencies at $\bar{M}$ for the Ar, Kr, and Xe Rayleigh waves calculated using models A and C_5.

TABLE XII. For the argon bilayer, we show frequencies at $\bar{\Gamma}$ and $\bar{M}$ calculated with model B, and with various versions of model C. The subscript on C in the various columns shows the number of neighbor shells included in the dynamical matrix.

Ar Bilayer $\bar{\Gamma}$	B	C_1	C_2	C_5	C_{10}
T_1, L_1	0.000	0.000	0.000	0.000	0.000
T_2, L_2	2.714	2.897	2.741	2.730	2.730
$\perp_1$	2.342	2.401	2.395	2.395	2.395
$\perp_2$	6.250	6.640	6.592	6.592	6.592
$\bar{M}$					
T_1	3.838	4.113	3.970	3.963	3.963
T_2	4.701	5.058	4.978	4.975	4.975
L_1	3.397	3.595	3.533	3.533	3.533
L_2	6.933	7.580	7.563	7.559	7.559
$\perp_1$	5.389	5.608	5.588	5.589	5.589
$\perp_2$	7.290	7.734	7.690	7.688	7.688

TABLE XIII. The normal mode frequencies at $\bar{M}$ using models A (B) and C_5 for the Rayleigh wave of bulk Ar, Kr, and Xe.

Adsorbate	A (B)	C_5
Ar	3.368	3.236
Kr	2.608	2.532
Xe	2.257	2.268

The last general consideration we discuss is the effect of relaxation normal to the substrate of the multilayer structure, within the framework of model C. In model C, the force constants will vary as the crystal relaxes, and this has the possibility of influencing the frequencies considerably. This can be seen by comparing the relaxed results [column C_5 (r)] and the unrelaxed results (column C_5) in Tables IV to IX. Changes in frequency as large as 10% can occur as a consequence of interlayer relaxation.

IV. DISCUSSION AND CONCLUDING REMARKS

A result of our comparison between the various models is that the overall structure of the dispersion curves is rather insensitive to the manner in which the lateral interactions between adsorbates is modeled; clearly use of the Lennard-Jones potential gives results substantially at variance with the other models explored, however. By and large, a nearest neighbor central force model, possibly with force constant calculated from the potential of Barker and co-workers, provides a description of the dispersion curves fully adequate to account for the data presently available. In fact, model C_5, which gives the best agreement with experiment, yields frequencies at $\bar{M}$ and $\bar{\Gamma}$ which are at most 6% higher than frequencies of model A for those modes which are detected in the experiments. Relaxation effects also have a modest influence on the phonon spectra. To repeat an earlier comment, we believe that coupling between the adatom and substrate atom motions is potentially more important than modest variations in the nature of the adatom–adatom potential. In our view, earlier work in the area has perhaps over-emphasized this last issue, though unambiguous determination of substrate-induced modifications to the lateral interactions between physisorbed atoms is surely an issue of fundamental interest. We now turn to a more detailed discussion of the comparison between theory and experiment.

The most sophisticated model used above is model C, where the phonon dispersion relations are calculated by constructing a dynamical matrix about a static configuration which minimizes the total energy of the model system. When the predictions of this model are compared with the data, there are in fact some significant discrepancies between the-

Downloaded 14 Sep 2004 to 143.106.6.126. Redistribution subject to AIP license or copyright, see http://jcp.aip.org/jcp/copyright.jsp

ory and experiment. For the Ar bilayer, the calculated width of the phonon band is distinctly too large, and we find a similar problem with all the trilayers.

The lattice constants we calculate by minimizing the total energy of model C are in fact slightly smaller than those measured in the experiment. This may be seen from Table X. The discrepancies are largest for the Ar bilayer, and all the trilayers, and it is in these cases we have the greatest difficulty fitting the phonon dispersion curves. In fact, in our model, we have omitted all three body contributions to both the static energy, and to the dynamical matrix used in the lattice dynamics. We have verified explicitly that the phonon frequencies are affected only very slightly by the inclusion of three body interactions. We have, for example, assessed the contribution of the Axilrod–Teller tripole dipole interaction, to find its contribution is quite negligible. However, from theoretical studies of bulk crystals, it is established that three body couplings are required to generate the proper lattice constant. Our problem here, if we wish to fully include them in the analysis, is that we have no information on noncentral force contributions to the energy that are unique to the adsorbed state. We envision three body interactions, in which one of the three entities is a substrate atom.

However, if it is indeed true that the phonon frequencies are influenced only very modestly by the three body couplings, then we may calculate phonon dispersion curves by simply using the *measured* lattice constant, rather than by using that provided by our energy minimization calculation. As seen from Table X, the experimental lattice constant is a bit larger than we calculate with our procedure. We argue that a small expansion of the lattice parallel to the surface is driven by three body interactions, and other lateral interactions ignored in our model. We have performed calculations using the experimental lattice constant, but with interlayer spacing relaxed in the manner provided by our model; this picture does not provide an optimum account of the data.

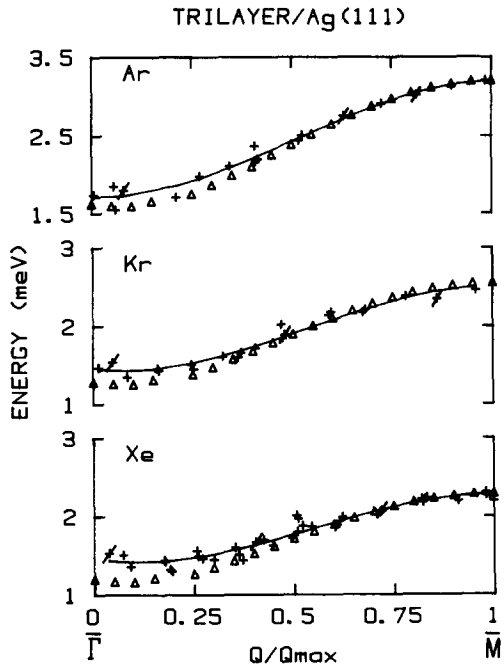

FIG. 8. A comparison between theory and experiment for the sequence of trilayers. The crosses are the experimental points. The slashes through selected crosses are indications of the error in the data. The solid line is a best fit to the data, while the triangles are obtained from the theory, assuming the modes L_1 and $\perp_1$ are responsible for the loss peak, as discussed earlier in the text.

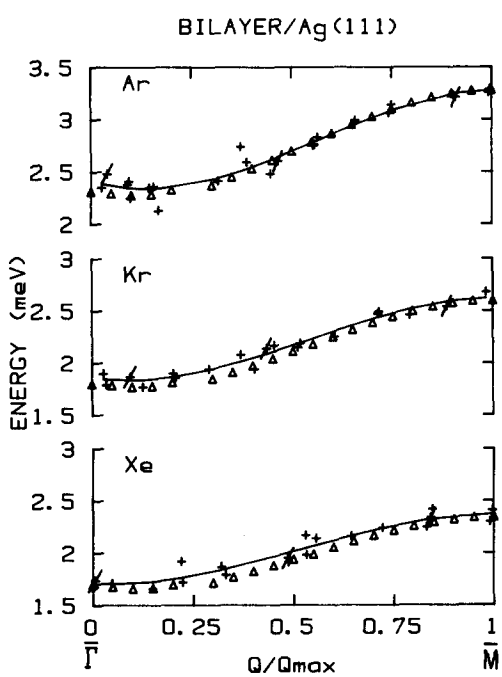

FIG. 7. A comparison between theory and experiment for the three bilayers. The crosses are the experimental points. The slashes through selected crosses are indications of the error in the data. The solid line is a best fit to the data, while the triangles are obtained from the theory, assuming the modes L_1 and $\perp_1$ are responsible for the loss peak, as discussed earlier in the text.

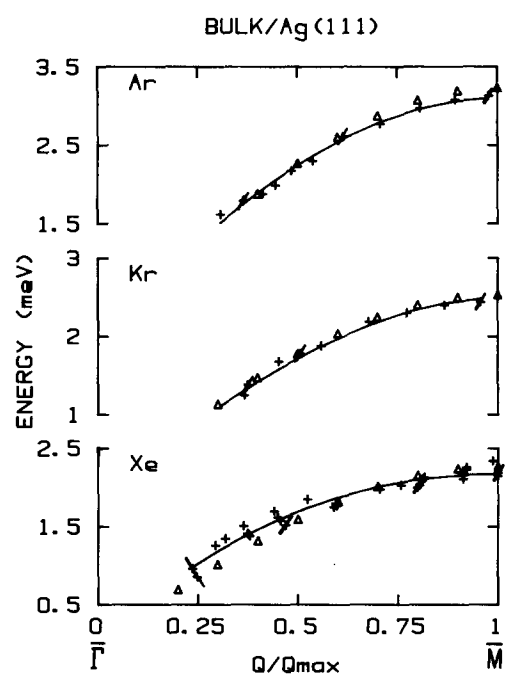

FIG. 9. A comparison between theory and experiment for a 25 layer slab. The crosses are the experimental points. The slashes through selected crosses are indications of the error in the data. The solid line is a best fit to the data, while the triangles are obtained from the theory.

Downloaded 14 Sep 2004 to 143.106.6.126. Redistribution subject to AIP license or copyright, see http://jcp.aip.org/jcp/copyright.jsp

TABLE XIV. Values of $|e_z|^2$, the square of the eigenvector component normal to the surface, for Ar bilayer, trilayer, and 25 layer films (Rayleigh wave only). In the case of the monolayer, $|e_z|^2$ is equal to 1 for the $\perp$ mode, and 0 for the other modes.

Q/Q_{max}	0	0.1	0.2	0.3	0.4	0.5	0.6	0.7	0.8	0.9	1.0
Mode						Bilayer					
T_1	0.0000	0.0000	0.0000	0.0000	0.0000	0.0000	0.0000	0.0000	0.0000	0.0000	0.0000
T_2	0.0000	0.0000	0.0000	0.0000	0.0000	0.0000	0.0000	0.0000	0.0000	0.0000	0.0000
L_1	0.0000	0.0029	0.0512	0.6776	0.7364	0.7669	0.7969	0.8287	0.8601	0.8849	0.8945
L_2	0.0000	0.1042	0.0839	0.0635	0.0549	0.0592	0.0912	0.0992	0.0625	0.0479	0.0453
$\perp_1$	0.7530	0.6479	0.6264	0.0321	0.0014	0.0025	0.0240	0.0656	0.0756	0.0655	0.0596
$\perp_2$	0.2470	0.2450	0.2385	0.2268	0.2073	0.1715	0.0879	0.0065	0.0018	0.0017	0.0006
						Trilayer					
T_1	0.0000	0.0000	0.0000	0.0000	0.0000	0.0000	0.0000	0.0000	0.0000	0.0000	0.0000
T_2	0.0000	0.0000	0.0000	0.0000	0.0000	0.0000	0.0000	0.0000	0.0000	0.0000	0.0000
T_3	0.0000	0.0000	0.0000	0.0000	0.0000	0.0000	0.0000	0.0000	0.0000	0.0000	0.0000
L_1	0.0000	0.0109	0.4477	0.5342	0.5720	0.6121	0.6585	0.7097	0.7583	0.7931	0.8056
L_2	0.0000	0.1032	0.0847	0.0848	0.1202	0.1069	0.0627	0.0503	0.0344	0.0123	0.0001
L_3	0.0000	0.0002	0.0034	0.0234	0.0535	0.0099	0.0002	0.0039	0.0029	0.0009	0.0000
$\perp_1$	0.5601	0.4511	0.0498	0.0001	0.0173	0.1261	0.1867	0.1818	0.1661	0.1596	0.1609
$\perp_2$	0.3395	0.3353	0.3186	0.2680	0.1577	0.0818	0.0534	0.0302	0.0108	0.0055	0.0046
$\perp_3$	0.1004	0.0993	0.0958	0.0895	0.0794	0.0633	0.0385	0.0241	0.0276	0.0286	0.0288
						Bulk					
S_1	0	0.0870	0.1309	0.2018	0.2959	0.3996	0.5019	0.5934	0.6654	0.7113	0.7271

The best agreement is found by using the experimental lattice constant, but then choosing an interlayer spacing appropriate to a perfect fcc lattice. The lack of vertical relaxation has its likely origin in screening of the holding potential by the inner adsorbate layers, the interlayer spacing may be expanded a bit for the same reason (e.g., three body interactions) as the two-dimensional unit cell is expanded. It is possible that a small amount of interlayer relaxation is present; the present precision in the data permits no clear conclusion on this point. This picture provides an excellent fit to the data. In Fig. 7, we show a comparison between theory and experiment, for the three bilayer systems. The crosses are the data points, the solid line a best fit to the data, and the triangles are provided by the theory, assuming the L_1 and $\perp_1$

TABLE XV. Values of $|e_z|^2$, the square of the eigenvector component normal to the surface, for Kr bilayer, trilayer, and 25 layer films (Rayleigh wave only). In the case of the monolayer, $|e_z|^2$ is equal to 1 for the $\perp$ mode, and 0 for the other modes.

Q/Q_{max}	0	0.1	0.2	0.3	0.4	0.5	0.6	0.7	0.8	0.9	1.0
Mode						Bilayer					
T_1	0.0000	0.0000	0.0000	0.0000	0.0000	0.0000	0.0000	0.0000	0.0000	0.0000	0.0000
T_2	0.0000	0.0000	0.0000	0.0000	0.0000	0.0000	0.0000	0.0000	0.0000	0.0000	0.0000
L_1	0.0000	0.0032	0.0734	0.6793	0.7237	0.7526	0.7825	0.8150	0.8480	0.8746	0.8851
L_2	0.0000	0.0855	0.0770	0.0608	0.0539	0.0605	0.1035	0.0981	0.0596	0.0458	0.0433
$\perp_1$	0.7369	0.6503	0.5950	0.0174	0.0003	0.0054	0.0371	0.0841	0.0901	0.0770	0.0699
$\perp_2$	0.2631	0.2610	0.2545	0.2426	0.2221	0.1815	0.0770	0.0028	0.0023	0.0026	0.0017
						Trilayer					
T_1	0.0000	0.0000	0.0000	0.0000	0.0000	0.0000	0.0000	0.0000	0.0000	0.0000	0.0000
T_2	0.0000	0.0000	0.0000	0.0000	0.0000	0.0000	0.0000	0.0000	0.0000	0.0000	0.0000
T_3	0.0000	0.0000	0.0000	0.0000	0.0000	0.0000	0.0000	0.0000	0.0000	0.0000	0.0000
L_1	0.0000	0.0122	0.4552	0.5246	0.5618	0.6022	0.6495	0.7018	0.7513	0.7864	0.7989
L_2	0.0000	0.0980	0.0839	0.0861	0.1242	0.1030	0.0633	0.0539	0.0384	0.0148	0.0010
L_3	0.0000	0.0003	0.0048	0.0299	0.0553	0.0062	0.0011	0.0045	0.0029	0.0009	0.0000
$\perp_1$	0.5486	0.4437	0.0325	0.0001	0.0253	0.1429	0.1935	0.1851	0.1686	0.1634	0.1663
$\perp_2$	0.3453	0.3407	0.3221	0.2642	0.1489	0.0780	0.0520	0.0300	0.0112	0.0064	0.0056
$\perp_3$	0.1061	0.1050	0.1015	0.0951	0.0847	0.0676	0.0406	0.0247	0.0277	0.0281	0.0282
						Bulk					
S_1	0	0.0872	0.1317	0.2030	0.2969	0.4003	0.5024	0.5938	0.6659	0.7119	0.7277

Downloaded 14 Sep 2004 to 143.106.6.126. Redistribution subject to AIP license or copyright, see http://jcp.aip.org/jcp/copyright.jsp

TABLE XVI. Values of $|e_z|^2$, the square of the eigenvector component normal to the surface, for Xe bilayer, trilayer, and 25 layer films (Rayleigh wave only). In the case of the monolayer, $|e_z|^2$ is equal to 1 for the $\perp$ mode, and 0 for the other modes.

Q/Q_{max}	0	0.1	0.2	0.3	0.4	0.5	0.6	0.7	0.8	0.9	1.0
Mode						Bilayer					
T_1	0.0000	0.0000	0.0000	0.0000	0.0000	0.0000	0.0000	0.0000	0.0000	0.0000	0.0000
T_2	0.0000	0.0000	0.0000	0.0000	0.0000	0.0000	0.0000	0.0000	0.0000	0.0000	0.0000
L_1	0.0000	0.0032	0.0622	0.6801	0.7354	0.7664	0.7968	0.8288	0.8604	0.8851	0.8947
L_2	0.0000	0.1273	0.0926	0.0675	0.0571	0.0607	0.0922	0.0972	0.0615	0.0471	0.0442
$\perp_1$	0.7529	0.6245	0.6067	0.0258	0.0008	0.0031	0.0274	0.0690	0.0769	0.0661	0.0599
$\perp_2$	0.2471	0.2450	0.2384	0.2266	0.2067	0.1698	0.0836	0.0050	0.0013	0.0017	0.0011
						Trilayer					
T_1	0.0000	0.0000	0.0000	0.0000	0.0000	0.0000	0.0000	0.0000	0.0000	0.0000	0.0000
T_2	0.0000	0.0000	0.0000	0.0000	0.0000	0.0000	0.0000	0.0000	0.0000	0.0000	0.0000
T_3	0.0000	0.0000	0.0000	0.0000	0.0000	0.0000	0.0000	0.0000	0.0000	0.0000	0.0000
L_1	0.0000	0.0121	0.4507	0.5303	0.5690	0.6096	0.6564	0.7078	0.7565	0.7914	0.8040
L_2	0.0000	0.1192	0.0909	0.0883	0.1202	0.1011	0.0629	0.0511	0.0346	0.0123	0.0001
L_3	0.0000	0.0002	0.0032	0.0217	0.0480	0.0086	0.0003	0.0038	0.0027	0.0008	0.0000
$\perp_1$	0.5581	0.4320	0.0392	0.0002	0.0225	0.1347	0.1892	0.1835	0.1678	0.1612	0.1625
$\perp_2$	0.3419	0.3375	0.3207	0.2706	0.1616	0.0837	0.0541	0.0308	0.0015	0.0065	0.0057
$\perp_3$	0.1000	0.0989	0.0953	0.0890	0.0787	0.0622	0.0370	0.0231	0.0270	0.0277	0.0278
						Bulk					
S_1	0	0.0878	0.1329	0.2042	0.2976	0.4004	0.5019	0.5928	0.6645	0.7104	0.7262

modes are responsible for the loss feature, as described earlier. Fig. 8 shows a similar comparison for the three trilayers, and Fig. 9 for the 25 layer slab. We also in Tables XIV–XVI (again using the experimental lattice constants), the values of $|e_z|^2$ for the various modes that 2, 3, and 25 layer films of Ar, Kr, and Xe/Ag(111) have along the $\bar{\Gamma}$–$\bar{M}$ direction.

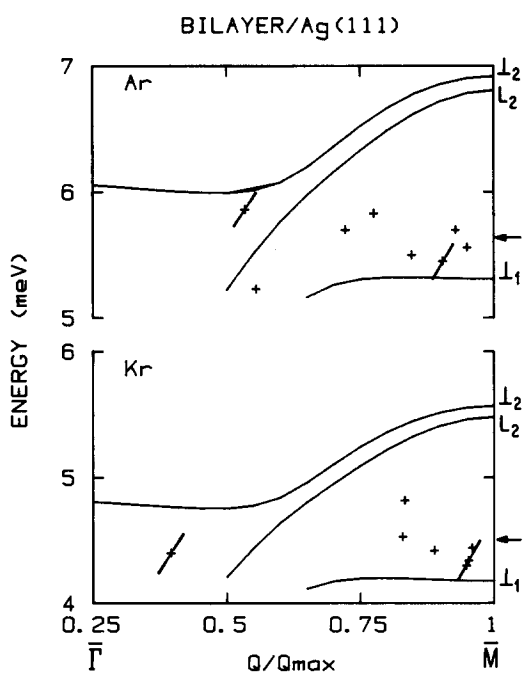

FIG. 10. The dispersion relation of the high frequency loss features near $\bar{M}$, observed for both the argon and the krypton bilayers. Superimposed on the data (crosses) are the dispersion relations of the $\perp_1$, $\perp_2$, and L_2 modes; the arrows indicate the value of the frequency $\bar{\omega}$ defined in the text.

The most significant discrepancy between theory and experiment occurs for the xenon trilayer, where the theory systematically falls below the data, in the vicinity of $\bar{\Gamma}$. We have no clear suggestion to offer about the origin of this difference, which amounts to roughly 0.2 meV for the data closest to $\bar{\Gamma}$. We are investigating the possibility that coupling between the substrate and adsorbate motions may raise the frequency of the adsorbate modes near $\bar{\Gamma}$.

For the Ar and Kr bilayer, a weak loss feature is observed at frequencies considerably higher than the range covered by Fig. 7. The structure is seen near the $\bar{M}$ point for both cases. In Fig. 10, the crosses indicate these features, and on the plot we superimposed the dispersion relations of the $\perp_1$ and L_2 modes, both of which have displacement components normal to the surface, and thus can be expected to produce loss features in this spectral range. In fact, when we calculate $|e_z|^2$, the square of the eigenvector component normal to the surface for the outermost adsorbate layer, the two are comparable in magnitude for these two modes. Thus, we argue the loss feature is produced by the combined action of these two eigenmodes, and is an unresolved doublet. If we construct a single loss feature by superimposing two rather diffuse Lorentzians, and assume the integrated strength of each scales like the square of the eigenvector $|e_z|^2$, we expect the peak of the resulting structure to occur at the frequency

$$\bar{\omega} = (\omega_1|e_z^{(1)}|^2 + \omega_2|e_z^{(2)}|^2)/2\ (|e_z^{(1)}|^2 + |e_z^{(2)}|^2)\ .$$

For the argon and krypton bilayer, the frequency $\bar{\omega}$ at $\bar{M}$ is indicated by an arrow placed on the plot. The frequencies weighted in this fashion are in very good accord with the position of the two loss features at $\bar{M}$. At $Q/Q_{max} = 0.5$, $\perp_2$ has the largest value of $|e_z|^2$.

In our view, a very intriguing aspect of the present work

Downloaded 14 Sep 2004 to 143.106.6.126. Redistribution subject to AIP license or copyright, see http://jcp.aip.org/jcp/copyright.jsp

is that it shows vividly how the Rayleigh wave of the semi-infinite solid evolves, as a function of layer thickness, out of the normal modes of a simple monolayer.[19,20] This is illustrated very beautifully in Fig. 3. The Rayleigh wave on the semi-infinite solid is always an admixture of motions parallel to, and normal to the surface. For the monolayer, with lateral interactions of central force character only, the normal modes are polarized either parallel to the surface (two branches), or normal to the surface, when coupling to substrate motions is ignored. Thus, since He atoms scatter predominantly from the normal component of displacement, we see the virtually dispersionless monolayer mode in Fig. 3. For mutilayer structures, except at high symmetry points, the modes polarized in the sagittal plane have mixed character, except at the high symmetry points. The mode that evolves into the Rayleigh wave acquires dispersion, and the frequency at $\overline{\Gamma}$ drops monotonically as the film thickness decreases, to zero in the limit of infinite thickness. If we consider a thick film, with thickness d, then the dispersion relation of the low frequency Rayleigh mode will track that appropriate to the solid in the regime where $\mathbf{Q}_{\parallel} d \gg 1$, where $\mathbf{Q}_{\parallel}$ is the wave vector of the wave, parallel to the surface. In this regime, the wave is sufficiently localized to the adlayer/vacuum interface that it does not "feel" the adlayer/substrate interface. When $\mathbf{Q}_{\parallel} d$ becomes the order of unity, then the wave penetrates deeply enough to feel the adlayer/substrate interface, and its frequency saturates to a finite value. At $\mathbf{Q}_{\parallel} = 0$, we have a pure $\hat{z}$ polarized mode, and one may argue (for a film many atomic layers thick) that its frequency should be $\pi c_t/2d$, where c_t is the appropriate transverse sound velocity. If we apply this simple formula to the trilayer and the bilayer, then as $\mathbf{Q}_{\parallel} \rightarrow 0$, the ratio of the frequency of the trilayer mode to that of the bilayer would be predicted to be 2/3, which is remarkably close to the ratio we see in Fig. 3.

In summary, we have investigated the surface phonon spectroscopy of rare gas overlayers adsorbed on Ag(111) using inelastic He scattering as the dynamical probe. This was done on a layer-by-layer basis for 1, 2, 3, and 25 layer (111) oriented films of Ar, Kr, and Xe. The monolayers exhibited a dispersionless Einstein oscillator mode, with the rare gas atoms vibrating in an uncorrelated manner in the holding potential of the Ag substrate. As progessively more layers were added, the observed modes showed increasing dispersion, until at 25 layers a bulklike Rayleigh mode was observed. This evolution is due to the increase in surface-to-substrate distance as the film gets progressively thicker, making the Ag–rare gas interaction less important with respect to the weaker rare gas–rare gas potential in determining the dynamical behavior of the surface. The experimental results were compared with lattice dynamics calculations using realistic rare gas pair potentials derived from gas phase experiments, and a Ag–rare gas potential derived in part from the observed monolayer frequencies. It is important to note that only the laterally averaged Ag–rare gas potential is necessary, since all of these rare gas systems are translationally incommensurate with respect to the Ag substrate. When all layers are coupled to the substrate, and the rare gas–rare gas interactions are modeled with a realistic gas phase pair potential summed over all neighbors necessary for convergence, very good agreement is reached between theory and experiment.

ACKNOWLEDGMENTS

The research of two of us (BH and DLM) has been supported by the Department of Energy, through Grant No. DE-FG-03-84ER-45083. That of JEB is supported by the National Science and Research Council of Canada, and the experimental work was supported, in part, by grants to S. J. S. from the U. S. Office of Naval Research (Grant No. ONR-N00014-77-C-0240), the Materials Research Laboratory Program of the National Science Foundation at the University of Chicago (Grant No. NSF DMR-79244007), and a Camille and Henry Dreyfus Young Faculty Grant.

[1] J. P. Toennies, J. Vac. Sci. Technol. A **2**, 1055 (1984).
[2] J. P. McTague, M. Nielsen, and L. Passel, in *Chemistry and Physics of Solid Surfaces*, edited by R. Vanselow (Chemical Rubber, Cleveland, 1979), Vol. 2.
[3] S. Lehwald, J. M. Szeftel, H. Ibach, T. S. Rahman, and D. L. Mills, Phys. Rev. Lett. **50**, 518 (1983).
[4] J. M. Szeftel, S. Lehwald, H. Ibach, T. S. Rahman, J. E. Black, and D. L. Mills, Phys. Rev. Lett. **51**, 268 (1983).
[5] B. F. Mason, K. McGreer, and B. R. Williams, Surf. Sci. **130**, 282 (1983).
[6] See Table 4.3, H. Ibach and D. L. Mills, *Electron Energy Loss Spectroscopy and Surface Vibrations* (Academic, New York, 1982), p. 451.
[7] J. Unguris, L. W. Bruch, E. R. Moog, and M. B. Webb, Surf. Sci. **87**, 415 (1979).
[8] J. Unguris, L. W. Bruch, E. R. Moog, and M. B. Webb, Surf. Sci. **109**, 522 (1981).
[9] L. Dobrzynski and D. L. Mills, J. Phys. Chem. Solids **30**, 1043 (1969); G. P. Alldredge, R. E. Allen, and F. W. de Wette, Phys. Rev. B **4**, 1682 (1971); W. R. Lawrence and R. E. Allen, *ibid.* **14**, 2910 (1976); **15**, 5081 (1977).
[10] B. Hall, D. L. Mills, and J. E. Black (to be published).
[11] K. D. Gibson and S. J. Sibener (to be published).
[12] G. Vidali, M. W. Cole, and J. R. Klein, Phys. Rev. B **28**, 3064 (1983).
[13] J. Unguris, L. W. Bruch, M. B. Webb, and J. M. Phillips, Surf. Sci. **114**, 219 (1982).
[14] E. Zaremba and W. Kohn, Phys. Rev. B **13**, 2270 (1976).
[15] J. A. Barker, R. A. Fisher, and R. O. Watts, Mol. Phys. **21**, 657 (1971).
[16] J. A. Barker, M. L. Klein, and M. V. Bobetic, IBM J. Res. Dev. **20**, 222 (1976).
[17] L. W. Bruch, Surf. Sci. **125**, 194 (1983).
[18] M. L. Klein and J. A. Venables, *Rare Gas Solids* (Academic, New York, 1976), Vol. I, p. 40.
[19] K. D. Gibson and S. J. Sibener, J. Vac. Sci. Technol. (in press).
[20] K. D. Gibson and S. J. Sibener, Phys. Rev. Lett. (submitted).

Downloaded 14 Sep 2004 to 143.106.6.126. Redistribution subject to AIP license or copyright, see http://jcp.aip.org/jcp/copyright.jsp